Effects of Scatter Correction on the Measurement of Infarct Size from SPECT Cardiac Phantom Studies

Michael K. O'Connor, Carlo Caiati, Timothy F. Christian and Raymond J. Gibbons

Departments of Radiology and Cardiology, Mayo Clinic, Rochester, Minnesota; and Division of Cardiology, Fondazione Clinica del Lavoro, Cassano Murge, Bari, Italy

Thallium-201 and ^{99m}Tc-sestamibi images of the heart contain a significant amount of scattered events which degrade image quality. Newer generation gamma cameras exhibit enhanced energy resolution and hardware/software to perform scatter correction. The principal aim of this study was to evaluate the effects of these advances in instrumentation on the quantitation of defect size from tomographic images of the heart obtained from a cardiac phantom. **Methods:** Tomographic images of a cardiac phantom containing no defect and defects of 5%–70% of total myocardial mass were acquired both with and without scatter correction for ^{201}Tl and ^{99m}Tc studies. Data were acquired on a newer generation gamma camera with an energy resolution of 8.7% at 140 keV. From conventional short-axis slices of the heart, circumferential count profiles were generated from five representative slices. Defect size was computed from the fraction of radians that fell below a fixed threshold value in each of the five count profiles. The nadir value (min/max) of the count profiles in each study was used as an index of image contrast. **Results:** For both ^{201}Tl and ^{99m}Tc, threshold values between 55%–60% gave the best correlation (r>0.99), with the lowest average absolute error in estimating defect size (<2.1%). Scatter correction reduced the average absolute error to 0.8% for ^{99m}Tc and 1.4% for ^{201}Tl, significantly reduced the nadir values for both isotopes (p<0.0001 for both ^{201}Tl and ^{99m}Tc and led to a marked improvement in image quality for both tracers. **Conclusion:** Scatter correction reduces the error associated with measurement of infarct size, increases image contrast and improves image quality for both ^{201}Tl and ^{99m}Tc, as assessed in a phantom model.

Key Words: myocardial infarct size; single-photon emission computed tomography; scatter correction; energy resolution

J Nucl Med 1995; 36:2080–2086

Tomographic images of the heart obtained using either ^{201}Tl or ^{99m}Tc-based radiopharmaceuticals contain a significant number of events that have undergone scattering either within the patient or in the collimator. The amount of scatter present in such studies is dependent on a large number of parameters, including gamma ray energy, thickness of absorber, width and offset of energy window and energy resolution of the imaging system (*1*). Previous work has shown that in the older generation of gamma cameras (i.e., those with energy resolution in the range 12%–15%), scatter accounted for approximately 35% of counts recorded within the energy window for ^{99m}Tc studies, with this value increasing to approximately 60% for ^{201}Tl studies (*2,3*). This difference in scatter content is the primary cause of the poorer image quality obtained with ^{201}Tl compared with ^{99m}Tc.

A large number of techniques have been proposed to reduce or eliminate the scatter content of the image data (*4*). These techniques can be classified into three main groups: (a) those designed to limit detection of scattered events, e.g., asymmetrical energy window (*5,6*), (b) weighting of the detected events according to their energy to remove scatter, e.g., the energy-weighted acquisition technique (*7,8*) and (c) elimination of the scattered events through the use of multiple energy windows (*9–11*). Two techniques falling into this last group are now commercially available on some gamma camera systems.

The technique used in this study acquires spectral information on a pixel-by-pixel basis through the use of multiple energy windows (*4,11*). A physical model of the energy spectrum is used which contains two terms, one is the unscattered contribution and the second is the scattered contribution expressed as a sum of terms for different orders of Compton scattering. Both terms are convoluted with the system energy resolution. The total counts T(i) for each individual pixel are then assumed to be described by

$$T(i) = \sum_{k=1}^{n} a_k(i)\, S_k + b(i)U,$$

where U is the scatter free component with a contribution b(i) and S_k is the probability distribution that a photon has undergone k interactions. The term $a_k(i)$ is the unknown contribution for each scatter component S_k. In practice, 2 orders of Compton scattering (k = 2) are adequate because of the limited statistics and digitization of the energy spec-

trum. For each pixel, the measured count density T(i) is then fitted to the physical model to obtain an estimate of the unscattered component.

It has been shown that the presence of scatter can significantly influence quantitative or semiquantitative analysis of tomographic studies (12,13). Over the last 6 yr, the Nuclear Cardiology Laboratory at the Mayo Clinic has performed quantitative analysis of ^{99m}Tc-sestamibi tomographic images to assess myocardium at risk, infarct size and treatment efficacy in acute myocardial infarction (14–16). The methodology for measurement of infarct size has been validated in a cardiac phantom model (17) and is based upon analysis of circumferential count profiles generated from representative short-axis slices of the myocardium. The percent of the count profile falling below 60% of the maximum counts in the profile is used to calculate infarct size. In clinical studies, the results have demonstrated significant associations with ejection fraction (14,15), regional wall motion (18) and left ventricular volumes (19). This methodology was developed on standard single-headed gamma camera systems without any type of scatter correction techniques. Not surprisingly, the application of this methodology to ^{201}Tl studies has required an increase in the threshold value from 60% to 70%, primarily because of the increased scatter content in these images (20). Over the last several years, a number of technological advances in instrumentation have occurred that reduce scatter and can potentially affect any type of quantitative tomographic analysis. The principal advances are: (a) improved energy resolution, with some systems achieving values of 8%–10% at 140 keV and (b) implementation of scatter correction hardware/software on some of the newer gamma camera systems, with at least two manufacturers offering such correction modules on their systems. These advances are expected to minimize the differences in image quality between ^{201}Tl and ^{99m}Tc studies and improve image contrast, accuracy and the reliability of quantitative analysis (21).

This study replicates and expands on earlier studies that validated a quantitative technique to measure infarct size with both ^{201}Tl and ^{99m}Tc in a phantom model (17,20). The principal aim of this study was to evaluate the effects of improved energy resolution and scatter correction on image quality and contrast and on the quantitation of defect size from tomographic images of the heart obtained using a cardiac phantom.

MATERIALS AND METHODS

Cardiac Phantom

All studies were performed using a commercially available phantom (Model RH-2, Capintec, NJ). This phantom consisted of a Lucite body (30 × 20 cm) with two compartments containing wood powder to simulate the lungs, a Teflon rod to simulate the spine and a third central compartment in which a heart model could be positioned. The heart model consisted of right and left ventricles with separate compartments for the blood pool and myocardium. Myocardial wall thickness was uniformly 11 mm

throughout the myocardium. Various rubber inserts (defects) could be placed into the myocardial compartment to simulate infarcted myocardium. For this study, eight infarct sizes were evaluated, using defects with volumes of 5% to 70% of total myocardial volume. Small defects (≤30% of myocardial volume) were placed in the inferior or infero-lateral region and were designed to simulate infarcts resulting from occlusion of the right coronary artery. Larger defects (≥40% of myocardial volume) were placed in the antero-septal region, simulating infarcts resulting from occlusion of the left anterior descending artery. A previous phantom study from this laboratory found that, for a given defect, altering its location within the myocardium (e.g., anterior versus inferior) resulted in a small (3%–4%) variation in measurement of defect size (17).

Data Acquisition

All studies were performed with both ^{201}Tl and [99m]Tc. For each isotope, nine acquisitions were performed, one for each of the eight defects and one with no defect. For each acquisition, the cardiac phantom was positioned in the center of the SPECT imaging table and orientated as for a conventional tomographic study of the heart. For the study with no defect, 2 mCi of the appropriate isotope were placed in the central compartment to simulate background activity and 1.5 mCi were placed in the myocardium. These activities were found to give a myocardial-to-background ratio comparable to that seen in clinical studies (17). With the introduction of various defects, myocardial activity was reduced in proportion to defect size, while background activity was kept constant.

For the above acquisitions, care was taken to ensure that all activity was well mixed within the appropriate compartment and that no air bubbles were present in the myocardium. All acquisitions were performed using the first head of a dual-headed gamma camera system (Helix system, Elscint Ltd., Haifa, Israel) equipped with a low-energy, high-resolution collimator. For each acquisition, images were acquired over 30 views for 30 sec/view into a 64 × 64 matrix. Data were acquired over 180°, beginning at the 45° RAO and ending at the 45° LPO.

At each view, images were acquired using the scatter correction software available on the system (11). Briefly, for ^{99m}Tc, at each view counts were acquired into 16 energy windows spanning the energy spectrum from 105 to 161 keV in 3.5-keV increments. From these 16 image sets, two image sets were produced. The first set was a standard image set containing counts that fell within a 20% energy window centered on the 140-keV photopeak (WIN). The second set was a Compton-free image set (CFI) derived by decomposing the energy spectrum for each pixel into its scattered and unscattered components. This process was achieved by performing a least squares fit of the spectral distribution of counts for each pixel in the image to a physical model of the unscattered and scattered events (based on the Klein Nishina formula) (4). To reduce noise and improve statistical accuracy, a sliding square of pixels (5 × 5) was used. Similarly for ^{201}Tl, counts were acquired into 16 energy windows spanning the energy spectrum from 56 to 86 keV in 2-keV increments. From these image sets, both conventional and scatter-free image sets were produced.

Gamma camera energy resolution determines the proportion of scattered events that fall within the energy window. The energy resolution of the dual-head system (installed in 1993) was measured at 75 and 140 keV by acquiring the energy spectrum of a ^{201}Tl or ^{99m}Tc point source placed 200 cm in front of the uncollimated gamma camera. To the extent possible, all nearby objects
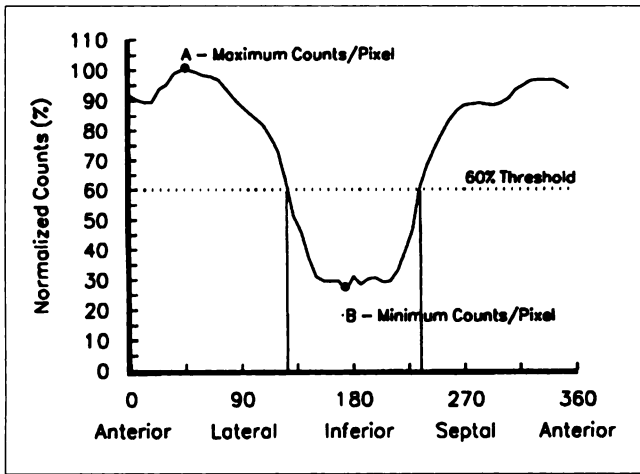
FIGURE 1. Schematic representation of a circumferential count profile from a short-axis slice demonstrates an antero-lateral defect. The fraction of the count profile that falls below the threshold value (set at 60% in this example) is used to compute the size of the defect, while the nadir (B/A) provides an estimate of image contrast for that defect.

that could contribute scatter to the detected radiation were removed. The energy spectrum was acquired in a similar manner on an older single-head gamma camera system (409 system, Elscint Ltd., Haifa, Israel, installed in 1989). Energy resolution was measured by determining the FWHM of the photopeak.

Data Analysis

For analysis, all data were transferred to a Pinnacle computer system (Medasys, Ann Arbor, MI). All datasets were reconstructed by prefiltering with a Hann filter (cut-off = 0.7 Nyquist) and backprojecting with a ramp filter. From the transaxial data, 6-mm thick short-axis slices of the heart were generated using the same orientation for all datasets and normalized to peak counts in the heart.

Since the same reconstruction parameters were used for all studies, short-axis slices from identical regions of the myocardium could be compared between different studies. Previous work from this laboratory has described extensively the methodology used to quantitate infarct size based on count profile analysis of the short-axis slices (14–17). Briefly, three short-axis slices were selected from the apex, midventricle and basal regions and two additional short-axis slices were selected midway between the mid-ventricle and the base and midway between the apex and midventricle. From these slices, circumferential count profiles were generated

by identifying the peak counts every 6° around the left ventricle. Measurement of defect size was determined from the fraction of radians (60 per slice) that fell below a fixed threshold of peak counts in each slice (Fig. 1). For both ^{99m}Tc and ^{201}Tl, we studied a range of threshold values from 45% to 75% in 5% increments. At each threshold value, the fraction of pixels that fell below that value were weighted by the slice radius. These fractions were summed to yield the fraction of the myocardium that was not perfused using a sum of cylinders technique (17). This analysis was performed on all nine studies at each threshold level for conventional and scatter-free image data from both radioisotopes. At each threshold level, the measured defect sizes from the nine studies were correlated with true defect size by regression analysis. The slope and intercept of the regression line were determined. The absolute error between the true and measured defect size was determined for each of the nine studies and the average value of this error used to determine the optimum threshold value.

In addition to measuring defect size, an index of image contrast was obtained in each study by measuring the nadir. Briefly from each of the five slices selected as described above, the minimum and maximum counts in the circumferential profile were determined and the ratio of minimum (B) to maximum (A) counts was calculated (Fig. 1). The smallest ratio (i.e., greatest drop in profile counts) from the five profiles was selected as the nadir. The nadir method has been previously described and used to assess defect severity in clinical studies (20). In theory, the nadir value should be 0% for all studies containing defects in the myocardium. In practice, scatter into the defect region will give a positive value for the nadir. Measurement of the nadir was performed for both isotopes with and without scatter correction.

RESULTS

The energy spectrum obtained from a point source under (relatively) scatter-free conditions for ^{201}Tl and ^{99m}Tc was significantly better on the dual-head system than on the older single-head system (Fig. 2). Energy resolution was measured at 8.7% for ^{99m}Tc and 15.9% for ^{201}Tl on the dual-head system. Comparable values for the single-head system were 12.1% and 19.2%, respectively. Following application of the scatter correction algorithm, the total counts in the scatter-free and conventional studies were determined. For ^{99m}Tc studies, the scatter-free studies showed a 35%–38% drop in counts relative to studies acquired with the standard energy window, while with ^{201}Tl studies, the drop in counts ranged from 25% to 28%.

Regression analysis correlating measured defect size with
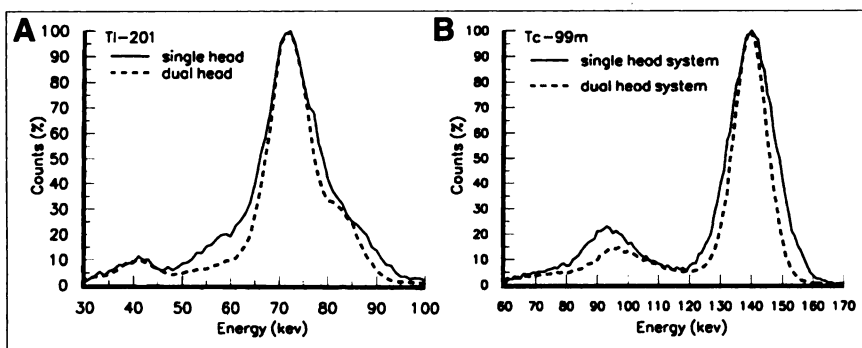
FIGURE 2. Energy spectra for (A) ^{201}Tl and (B) ^{99m}Tc point sources in air from head 1 of the dual-head and single-head systems.

FIGURE 3. Linear regression analysis compares true versus measured defect size as a function of the threshold value for (A) scatter corrected data (CFI) and (B) conventional image data (WIN) acquired with ^{99m}Tc.
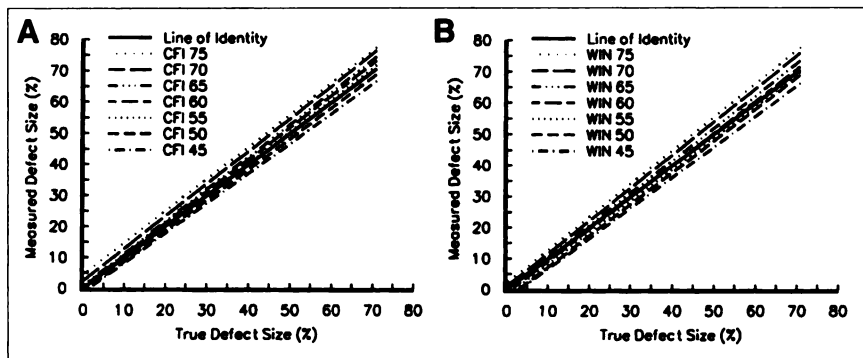
true defect size showed excellent correlation ($r>0.96$) for both isotopes with and without scatter correction (Figs. 3,4). Table 1 presents the values of the slopes, intercepts and correlation coefficients from the regression analysis for both ^{99m}Tc and ^{201}Tl, as well as the average absolute error between true and measured defect sizes. Because of the high correlation obtained at all threshold values, the average absolute error was used to determine the optimum threshold value. This parameter is shown in Figure 5 as a function of the threshold value for ^{99m}Tc and ^{201}Tl. For both isotopes, the minimum value of the average absolute error occurred between threshold values of 55%–60%. Scatter correction did not significantly alter the optimum threshold value but did result in significantly lower values of the average absolute error for both isotopes ($p<0.05$ for ^{99m}Tc; $p<0.001$ for ^{201}Tl).

The improvement in image quality with scatter correction can be seen in the vertical long-axis slices of the heart shown for the 30% defect with ^{99m}Tc and ^{201}Tl (Fig. 6). This improvement can be seen quantitatively from the nadir measurement, shown as a function of defect size for both ^{99m}Tc (Fig. 7A) and ^{201}Tl (Fig. 7B). Scatter correction resulted in a significant reduction in the nadir value, indicating improved contrast ($p<0.0001$ for both ^{201}Tl and ^{99m}Tc). For ^{99m}Tc scatter correction reduced the nadir value to zero for large defects. Similar results were obtained with ^{201}Tl, but the nadir value was significantly larger than that seen with ^{99m}Tc at all defect sizes ($p>0.0005$). For large anterior defects (40%–70%), the nadir was 2.1% ± 1.0% for ^{99m}Tc and 11.4% ± 5.2% for ^{201}Tl, reflecting the different scatter components of the two isotopes (Fig. 7).

For these large defects, scatter correction reduced the nadir to 0.2% ± 0.4% for ^{99m}Tc but only to 4.5% ± 2.0% for ^{201}Tl.

DISCUSSION

Our results show that an excellent correlation exists between true and measured defect size over a wide range of threshold values for ^{201}Tl and ^{99m}Tc. For ^{99m}Tc, a 60% threshold minimizes the average absolute error and represents the optimum threshold value for determining defect size. This result for ^{99m}Tc images acquired with a standard 20% energy window is similar to the value previously reported by this laboratory for ^{99m}Tc (14,17). Following scatter correction (Figs. 4, 5B), there was a reduction in the optimum threshold value to 55%, with a small but significant reduction in the average absolute error in estimating defect size.

The results for ^{201}Tl acquired with a conventional energy window showed a reduction in the optimum threshold value from a previously reported value of 70% (20) to a value of 60% (Fig. 5B). This reduction in threshold value may be due to the difference in energy resolution between the system used in this study and that used in previous studies. The previous value reported from this laboratory was obtained from data acquired on a conventional single-head system similar to that used to compare energy resolution in this study (Fig. 2A). This improvement (from 19% to 16% for ^{201}Tl) in energy resolution has been shown to reduce the amount of scatter falling within a standard energy window (21). Since ^{201}Tl images have a higher scatter content than

FIGURE 4. Linear regression analysis compares true versus measured defect size as a function of the threshold value for (A) scatter corrected data (CFI) and (B) conventional image data (WIN) acquired with ^{201}Tl.
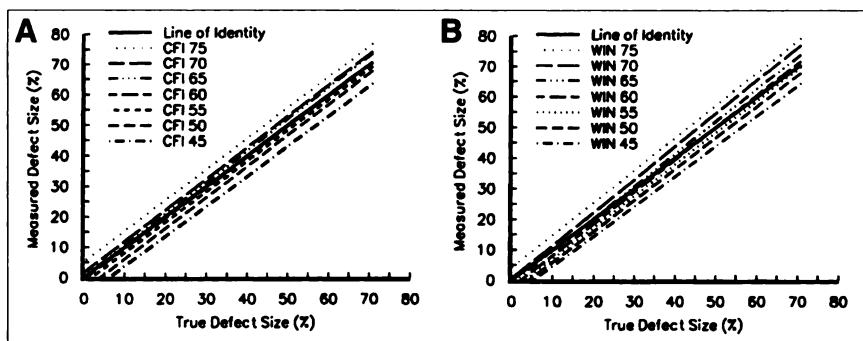
TABLE 1

True Versus Measured Defect Size: Regression Analysis Results for Technetium-99m and Thallium-201 as a Function of Scatter

| Isotope	Scatter correction	Threshold	Slope	Intercept	Correlation coeff. (R^2)	Average absolute error (mean ± s.d.)
^{99m}Tc	Yes	75	1.033	4.45	0.987	5.51 ± 3.11
		70	1.047	2.46	0.991	3.96 ± 2.80
		65	1.043	0.79	0.993	2.36 ± 2.28
		60	1.031	0.38	0.997	1.58 ± 1.43
		55	1.021	−0.38	0.999	0.78 ± 0.71
		50	0.991	−1.19	0.996	1.49 ± 1.59
		45	0.965	−1.48	0.996	2.60 ± 1.77
^{99m}Tc	No	75	1.069	2.18	0.989	4.40 ± 3.32
		70	1.061	1.00	0.993	3.13 ± 2.51
		65	1.040	−0.01	0.998	1.47 ± 1.25
		60	1.030	−1.12	0.996	1.42 ± 1.08
		55	1.015	−1.86	0.994	1.78 ± 1.61
		50	1.017	−2.93	0.995	2.56 ± 1.64
		45	0.983	−3.18	0.995	3.71 ± 1.76
^{201}Tl	Yes	75	1.010	5.23	0.985	5.62 ± 3.21
		70	1.027	1.64	0.994	2.51 ± 2.05
		65	1.040	0.12	0.994	1.60 ± 2.09
		60	1.004	−0.51	0.995	1.42 ± 1.17
		55	1.007	−1.95	0.995	2.11 ± 1.35
		50	1.017	−4.15	0.990	3.60 ± 2.67
		45	0.985	−6.11	0.975	6.60 ± 3.97
^{201}Tl	No	75	1.062	4.19	0.967	6.18 ± 5.18
		70	1.083	0.51	0.974	3.80 ± 4.41
		65	1.062	−1.02	0.990	2.27 ± 2.28
		60	1.051	−2.46	0.990	2.04 ± 2.17
		55	1.035	−3.39	0.990	2.89 ± 1.93
		50	1.022	−4.42	0.988	3.89 ± 2.61
		45	0.985	−5.34	0.980	5.82 ± 3.50

^{99m}Tc images, scatter correction may have a more profound effect on the optimum threshold value for ^{201}Tl than for ^{99m}Tc. Additional evidence for this can be seen in the value for the average absolute error in estimating defect size. This value was previously reported at >5% for ^{201}Tl (20), while in this study, the error was only 2% at the 60% threshold. The use of scatter correction did not alter the optimum threshold value but did lead to a further reduction in the average absolute error. Hence, for both isotopes, the primary effect of scatter correction appears to be improved accuracy in measuring defect size.

The improved image quality with scatter correction can be seen in the long-axis slices through the heart. Scatter correction also leads to improved image contrast, as evident in Figure 7, which measures the nadir values for the ^{99m}Tc and ^{201}Tl studies. As defect size decreases, however, the nadir increases, with this increase occurring more rapidly for ^{201}Tl than for ^{99m}Tc, despite the use of scatter correction. While this increase is partly due to partial volume effects, a discontinuity can be seen between the nadir values for ^{201}Tl at 30% and 40% (Fig. 7B), which was not observed for ^{99m}Tc (Fig. 7A). Coincidentally, this discontinuity corresponds to a change in defect location with defects 30% or smaller located in the inferior or infero-lateral wall, while those 40% or larger were located in the anterior wall. This finding is consistent with the known limitations of ^{201}Tl in
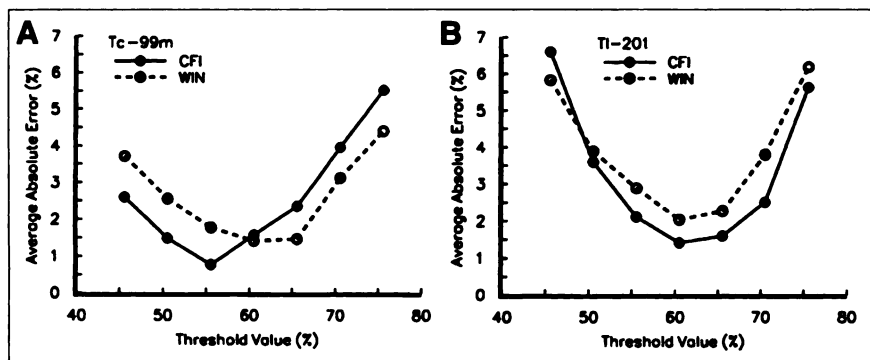
FIGURE 5. Average absolute error in estimating defect size as a function of the threshold value for scatter corrected (CFI) and conventional (WIN) image data acquired with (A) ^{99m}Tc and (B) ^{201}Tl.
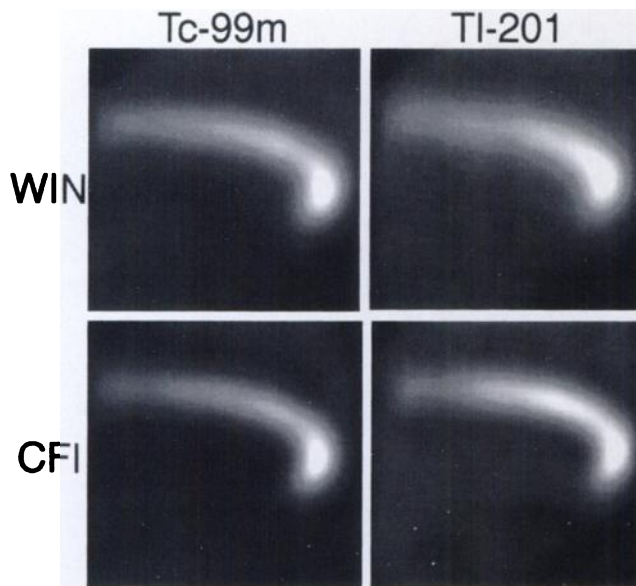
FIGURE 6. Vertical long-axis slices of the heart contain a 30% inferior defect for ^{99m}Tc and ^{201}Tl studies with (CFI) and without (WIN) scatter correction.

evaluating inferior wall defects (1,22,23). Although scatter correction improved image contrast, it did not eliminate this discontinuity. This may be due to a number of factors, including differences in spatial resolution and photon attenuation between ^{201}Tl and ^{99m}Tc and/or may reflect incomplete scatter correction of the ^{201}Tl image data. For the large anterior defects in scatter-free studies in which partial volume effects are not an issue, we would have expected the nadir values in the ^{201}Tl images to more closely match those seen in the ^{99m}Tc images. These nadir values, however, remain at about 5%. Furthermore, in comparing the total counts present in the scatter-free and conventional image sets, it would be expected that more counts would be removed from the ^{201}Tl data than from the ^{99m}Tc data due to the higher scatter content (2,3).

Our results showed the opposite effect, with a 35%–38% reduction in counts with ^{99m}Tc, but only a 25%–28% reduction with ^{201}Tl. These findings may indicate that the scatter correction technique is not adequately correcting for scatter, particularly in the ^{201}Tl images. There are a number

of possible explanations for this discrepancy. Other studies using curve fitting to parts of the energy spectrum have shown that the curve fit may still underestimate scatter in complex objects due to a failure to account for small angle scatter (24). Previous studies with this technique have demonstrated its ability to correct for scatter in simple objects (e.g., point source in water) but have only qualitatively evaluated its application in more complex objects and in clinical studies. The scatter-free imaging technique is based on a pixel-by-pixel spectral analysis of the data (11) and assumes that there are no local variations in the energy response of the gamma camera over the field of view and that this response is stable over time (4). The validity of these assumptions, in particular, the long-term stability of the system over time, has not been studied. Hence, while the above results are promising, further development and refinement are required to make this technique more robust.

While the limitations of this technique are evident, one of the most important outcomes from this study is the diminution of the qualitative and quantitative differences in image quality between ^{99m}Tc and ^{201}Tl. In clinical practice, this will better facilitate the use of dual-isotope studies and the comparison of clinical studies acquired with [^{201}Tl]thallous chloride and ^{99m}Tc-sestamibi. The concurrent development of attenuation correction techniques on many of the newer SPECT systems should further facilitate these types of studies.

CONCLUSION

This study shows that the combined effects of scatter correction and improvement in system energy resolution leads to a significant gain in image quality. In particular, there was reduction in the error associated with measurement of infarct size and an increase in image contrast for both ^{201}Tl and ^{99m}Tc. These gains in image quality minimized the differences in the quantitative analysis of ^{201}Tl and ^{99m}Tc studies and should better facilitate the use of dual-isotope studies and the comparison of clinical studies acquired on separate occasions with [^{201}Tl]thallous chloride and ^{99m}Tc-sestamibi.
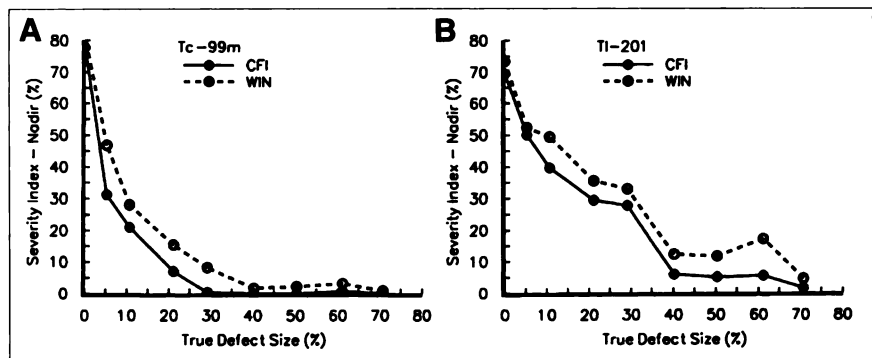
FIGURE 7. Effect of defect size on the measurement of the nadir with (CFI) and without scatter correction (WIN). Results are shown for (A) ^{99m}Tc and (B) ^{201}Tl.

REFERENCES

1. Budinger TF, Rollo D. *Physics and instrumentation.* In: Holman BL, Sonnenblick EH, Lesch M, eds. *Principles of cardiovascular nuclear medicine.* New York: Grune and Stratton; 1978:17-52.
2. Anger HO. Radioisotope Cameras. In: Hine GJ, ed. *Instrumentation in nuclear medicine, vol. 1.* New York: Academic Press; 1967:485-552.
3. Jaszczak RJ, Greer KL, Floyd CE, Harris CC, Coleman RE. Estimating SPECT count densities, scatter fractions, and statistical noise. *IEEE Trans Nucl Sci* 1985;NS-32:762-768.
4. Buvat I, Benali H, Todd-Pokropek A, Di Paola R. Scatter correction in scintigraphy: the state of the art. *Eur J Nucl Med* 1994;21:675-694.
5. Collier BD, Palmer DW, Knobel J, Isitman AT, Hellman RS, Zielonka JS. Gamma camera energy windows for Tc-99m bone scintigraphy: effect of asymmetry on contrast resolution. *Radiology* 1984;151:495-497.
6. Graham LS, La Fontaine RL, Stein MA. Effects of asymmetric photopeak windows on flood field uniformity and spatial resolution of scintillation cameras. *J Nucl Med* 1986;27:706-713.
7. Halama JR, Henkin RE, Friend LE. Gamma camera radionuclide images: improved contrast with energy-weighted acquisition. *Radiology* 1988;169:533-538.
8. DeVito RP, Hamill JJ. Determination of weighting functions for energy-weighted acquisition. *J Nucl Med* 1991;32:343-349.
9. Ichihara T, Ogawa K, Motomura N, Kubo A, Hashimoto S. Compton scatter compensation using the triple-energy window method for single- and dual-isotope SPECT. *J Nucl Med* 1993;34:2216-2221.
10. Ljungberg M, King MA, Hademenos GJ, Strand SE. Comparison of four scatter correction methods using Monte Carlo simulated source distributions. *J Nucl Med* 1994;35:143-151.
11. Berlad G, Maor D, Natanzon A, Shrem Y, Todd-Pokropek A. Compton-free imaging (CFI): validation of a new scatter correction method [Abstract]. *J Nucl Med* 1994;35:143P.
12. Galt JR, Cullom JC, Garcia EV. SPECT quantification: a simplified method of attenuation and scatter correction for cardiac imaging. *J Nucl Med* 1992;33:2232-2237.
13. Meikle SR, Hutton BF, Bailey DL. A transmission-dependent method for scatter correction in SPECT. *J Nucl Med* 1994;35:360-367.
14. Gibbons RJ, Verani MS, Behrenbeck T, et al. Feasibility of tomographic 99mTc-hexakis-2-methoxy-2-methylpropyl-isonitrile imaging for the assess-ment of myocardial area at risk and the effect of treatment in acute myocardial infarction. *Circulation* 1989;80:1277-1286.
15. Christian TF, Behrenbeck T, Pellikka PA, Huber KC, Chesebro JH, Gibbons RJ. Mismatches of left ventricular function and perfusion with Tc-99m-isonitrile following reperfusion therapy for acute myocardial infarction: identification of myocardial stunning and hyperkinesia. *J Am Coll Cardiol* 1990; 16:1632-1638.
16. Behrenbeck T, Pellikka PA, Huber KC, et al. Primary angioplasty in myocardial infarction: assessment of improved myocardial perfusion with technetium-99m isonitrile. *J Am Coll Cardiol* 1991;17:1-7.
17. O'Connor MK, Hammel T, Gibbons RJ. In vitro validation of a simple tomographic technique for estimation of percentage myocardium at risk using methoxyisobutyl isonitrile technetium-99m (sestamibi). *Eur J Nucl Med* 1990;17:69-76.
18. Gibson RS, Watson DD, Craddock GB, et al. Prediction of cardiac events after uncomplicated myocardial infarction: a prospective study comparing predischarge exercise thallium-201 scintigraphy and coronary angiography. *Circulation* 1983;68:321-336.
19. Christian TF, Behrenbeck T, Gersh BJ, Gibbons RJ. Relation of left ventricular volume and function over one year following acute myocardial infarction to infarct size determined by Tc-99m sestamibi. *Am J Cardiol* 1991;17:365-372.
20. Christian TF, O'Connor MK, Hopfenspirger MR, Gibbons RJ. Comparison of reinjection thallium-201 and resting technetium-99m sestamibi tomographic images for the quantification of infarct size after acute myocardial infarction. *J Nucl Cardiol* 1994;1:17-28.
21. Kojima A, Matsumoto M, Takahashi M, Uehara S. Effect of energy resolution on scatter fraction in scintigraphic imaging: Monte Carlo study. *Med Phys* 1993;20:1107-1113.
22. DePasquale E, Nody A, DePuey EG, et al. Quantitative rotational thallium-201 tomography for identifying and localizing coronary artery disease. *Circulation* 1988;77:316-327.
23. Van Train K, Maddahi J, Wong C, et al. Definition of normal limits in stress Tl-201 myocardial rotation tomography [Abstract]. *J Nucl Med* 1986;27:899.
24. Seidel J, Green MV, Daube-Witherspoon ME, Bacharach SL. Correction for compton scatter using the local scatter fraction to estimate small angle scatter [Abstract]. *J Nucl Med* 1994;35(suppl):143P.